ACS EARTH AND SPACE CHEMISTRY

http://pubs.acs.org/journal/aesccq

Article

Effect of Cations (Na^+, K^+, and Ca^{2+}) on Methane Hydrate Formation on the External Surface of Montmorillonite: Insights from Molecular Dynamics Simulation

Yun Li, Meng Chen, Hongzhe Song, Peng Yuan,* Baifa Zhang, Dong Liu, Huijun Zhou, and Hongling Bu

Cite This: *ACS Earth Space Chem.* 2020, 4, 572−582

Read Online

ACCESS | Metrics & More | Article Recommendations | Supporting Information

ABSTRACT: In this study, molecular dynamics simulations were performed to investigate the effects of montmorillonite with different surface cations (*i.e.*, Na^+, K^+, and Ca^{2+}) on CH_4 hydrate formation. The results showed that CH_4 hydrate cages are mainly formed beyond the montmorillonite surface. The inner-sphere adsorption of K^+ and the outer-sphere adsorption of Na^+ and Ca^{2+} occurred on the montmorillonite surface, leading to differences in order parameters and hydrogen bond number of H_2O molecules. The number of structure I cages increased faster than that of structure II cages in different models and were in agreement with the fact that CH_4 molecules can only form sI hydrate crystals. The number of 5^{12} cages increased in the order: Na−Mt < Ca−Mt < K−Mt. The aqueous environment dominated by K^+ on the external surface of montmorillonite facilitate heterogeneous nucleation of CH_4 hydrate rather than that by Ca^{2+} or Na^+. The abovementioned findings suggest that the coordination structure of cations on the external surface of montmorillonite plays an important role in CH_4 hydrate formation through altering the occupation of CH_4 hydrate.

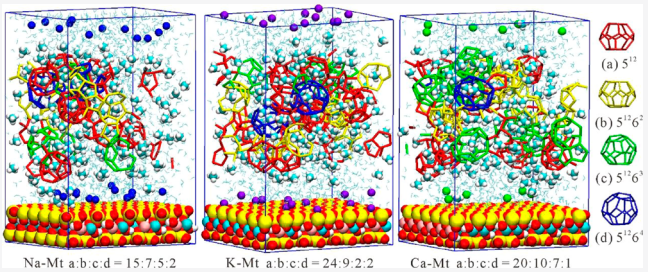

KEYWORDS: *CH_4 hydrate, montmorillonite, hydration structure, molecular dynamics simulation, surface cation*

INTRODUCTION

There has been sustained interest in CH_4 hydrate because of its large energy density and environmentally abundant nature as compared to other fossil fuels (*e.g.*, coal, oil, and natural gas).[1] CH_4 hydrate is vastly distributed in permafrost areas and marine sediments along the continental margins under high CH_4 concentration, medium pressure, and low temperature environments.[2,3] Structurally, CH_4 hydrate is an ice-like nonstoichiometric crystalline compound made up of CH_4 and H_2O molecules, CH_4 hydrate presents a cubic structure that consists of 46 H_2O molecules per unit cell, forming six $5^{12}6^2$ (12 pentagons and 2 hexagons) and two 5^{12} cages.[1,4]

Because of the enormous potential of CH_4 hydrate to be used in energy storage and geological applications, experimental and modeling studies have focused on the nucleation and growth mechanism of CH_4 hydrate.[5−7] It has been known that the formation kinetics of CH_4 hydrate is affected by geological and environmental conditions, such as mineral type,[8−11] organic matter,[12−14] and inorganic salt concentration.[15] Among them, clay minerals were regarded as an important variable because they are the main component in natural sediments.[10,16−19] According to previous studies, the formation of CH_4 hydrate in the presence of clay minerals differ from that of the bulk hydrate phase, which is because of the unique structure and surface chemistry of clay minerals.[16,17] For instance, Guggenheim and van Groos showed that a montmorillonite−CH_4 hydrate intercalate can be stably formed in the interlayer with a 1.2 nm interlayer distance upon pressurization at 41.4 bar. The stable upper limit of hydrate intercalate on the pressure and temperature was parallel to that of CH_4 hydrate, but the temperatures were 0.5−1 °C lower than that of CH_4 hydrate.[17] Cha *et al.* showed that the large specific surface areas of clay minerals provide nucleation sites to promote the CH_4 hydrate formation, and the stable temperature and pressure range of CH_4 hydrate in the presence of clay minerals was broader than that in H_2O alone.[20] Zhou *et al.* observed disordered clathrate-like structures in montmorillonite−CH_4 hydrate intercalate models and found that the behavior of the CH_4 hydrate complex in the interlayer was affected by the amount of intercalated H_2O.[21] The abovementioned studies all suggest that the presence of

Received: December 20, 2019
Revised: March 12, 2020
Accepted: March 19, 2020
Published: March 19, 2020

clay minerals is a crucial variable in governing the CH_4 hydrate formation. In view of the ubiquity of clay minerals in the geological environments where CH_4 hydrate is generated, it is of no doubt that further research work is warranted to evaluate the effects of clay minerals on the CH_4 hydrate formation.

Montmorillonite is one of the most widespread clay minerals in CH_4 hydrate-bearing sediments.[18−20] Montmorillonite is a 2:1 dioctahedral clay mineral with a layer composed of an octahedral sheet sandwiched between two opposing tetrahedral sheets. The isomorphic substitutions in the tetrahedral and octahedral sheets create the negative charge of the montmorillonite layer. The layer charge is primarily balanced by alkali and alkaline earth cations adsorbed onto basal surfaces or in the interlayer region of montmorillonite.[22,23] The role of montmorillonite in the CH_4 hydrate formation is currently a controversial subject because there are many issues that require clarification. For example, previous studies suggested that montmorillonite could promote the hydrate nucleation because of the specific surface area, and the promotion is caused by the surface-adsorbed H_2O molecules into ordered layers that approximate a part of hydrate lattices.[6,24] However, some experiments indicated that montmorillonite could inhibit gas hydrate formation by disrupting the hydrogen bond (HB) network of H_2O molecules. Therefore, in the presence of montmorillonite, higher pressure or a lower temperature was necessarily required to construct hydrate structures.[25,26] Studies on CH_4 hydrate formation in montmorillonite suspension have revealed a unique phase equilibrium condition of CH_4 hydrate, which was ascribed to an inhibition behavior by the capillary effect and surface interactions of nanopores (*i.e.*, interlayer space and interparticle space).[16,27] Despite the inconsistency between different studies, it has been well accepted that the structure and surface characteristics of montmorillonite must have played important roles in the gas hydrate formation in the natural sediments, but the underlying mechanism requires further investigation. Cations adsorbed onto the external surface of montmorillonite from salt solutions in an ambient environment is a crucial issue with respect to the CH_4 hydrate formation. Previous studies have reported that a low concentration of inorganic salts effectively promotes CH_4 hydrate formation, while a high concentration of inorganic salts inhibits it. At a low concentration of inorganic salts, large and polarizable anions are hydrophobic, and they will interact with surrounding H_2O molecules to form hydrophobic hydration shells. These hydration shells are similar to those of the hydration shells of CH_4 molecules, resulting in the promotion of CH_4 hydrate formation.[28,29] The inhibition of CH_4 hydrate formation at high salt concentrations was explained by the competition between cations and CH_4 molecules for H_2O molecules, as well as the distortion in the HB structure of H_2O molecules. It was found that smaller cations have a higher charge density, leading to stronger electronic interactions between cations and H_2O molecules. This will cause weak HB interactions between H_2O molecules. In contrast, large cations have a lower charge density, leading to H_2O molecules that more easily interacts with each other through the HB network.[30]

It is known that different types of inorganic salt ions (*e.g.*, Na^+, K^+, Ca^{2+}, Mg^{2+}, and Cl^-) exist in the pore H_2O of CH_4 hydrate-bearing sediments.[31] The negative charges of montmorillonite in natural sediments are compensated by the presence of inorganic ions in pore H_2O, located on the surface and the frayed edges of montmorillonite. The charge-dipole attraction between H_2O molecules and surface cations results in the unique chemical and physical characteristics of the montmorillonite surface under cation-rich environments. The distribution and hydration characteristics of cations on the external surface determine the hydrophilicity on the montmorillonite surface. H_2O molecules around cations on the montmorillonite surface are chemically and physically distinct from the bulk phase. More importantly, gas molecules introduced into the montmorillonite interacted with the H_2O molecule-solvating cations. Therefore, an important issue is raised, that is, how the external surface cations of montmorillonite influence the cage number, cage occupancy, and distribution of CH_4 hydrate during the CH_4 hydrate formation. Unfortunately, it is technically difficult to investigate the molecular mechanism of gas hydrate formation on the montmorillonite surface by phase equilibrium experiments.[32,33] In this scenario, the development of force fields for molecular simulation of clay minerals in recent years provides a powerful tool to study the interfacial behavior of montmorillonite at the molecular level.[34] Particularly, molecular dynamics (MD) simulations have been significant in studying the clay-fluid system and the gas hydrate in the presence of clay minerals.[35,36]

In this study, the formation of CH_4 hydrate in the presence of montmorillonite with different surface cations (Na^+, K^+, and Ca^{2+}) were investigated using MD simulations. The purpose of this study was to determine the effect of different cations on CH_4 hydrate formation at the external surface of montmorillonite. The structure and dynamics of H_2O molecules in different models were compared by analyzing the density profile, radial distribution function (RDF), and mean square displacement (MSD). The local order parameter and cage structure were investigated to gain a better understanding of the nucleation mechanism of CH_4 hydrate on the montmorillonite surface.

METHODOLOGY

Molecular Models. The molecular models of montmorillonite were derived from the pyrophyllite structure,[37] which was obtained from the American Mineralogist Crystal Structure Database.[38] The lattice parameters of the unit cell of pyrophyllite are as follows: a = 5.16 Å, b = 8.97 Å, and c = 9.37 Å, and α = 91.5°, β = 100.46°, and γ = 89.6°. To prepare the montmorillonite model, the layer charge was created primarily by the substitution of Mg^{2+} for Al^{3+} in the octahedral sheet, and the isomorphic substitutions obey Loewenstein's rule (*i.e.*, two substitution sites cannot be adjacent).[39] The Na^+, K^+, and Ca^{2+} were used to balance the negative layer charge. Thus, the chemical formula of montmorillonite is $M[Al_3Mg][Si_8O_{20}](OH)_4$, with M = Na^+, K^+, and Ca^{2+}. A 6 × 4 × 1 supercell model with l_x = 3.096 nm and l_y = 3.586 nm was created. The final orthorhombic model was obtained from the triclinic supercell model, which would not affect the simulation results.[40,41] Three montmorillonite models with different surface cations (*i.e.*, $24Na^+$, $24K^+$, and $12Ca^{2+}$) were created. A bulk solution model was generated including $140CH_4$ and $1610H_2O$ molecules, which were randomly distributed within a 3.096 nm × 3.586 nm × 5 nm simulation box. The CH_4 molar fraction was 0.08 in this study, about half of that in the CH_4 hydrate crystal, and thus not all the H_2O molecules could convert into CH_4 hydrate. Additionally, the CH_4 molar fraction satisfied the condition that the CH_4 molecules would remain uniformly distributed in the liquid H_2O without

https://dx.doi.org/10.1021/acsearthspacechem.9b00323
ACS Earth Space Chem. 2020, 4, 572−582

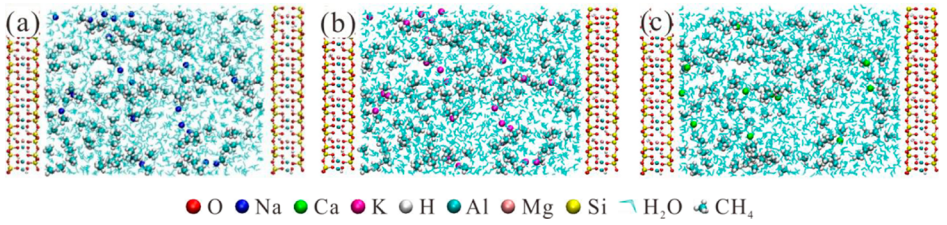

Figure 1. Initial configuration of the simulation models. (a) Na−Mt, (b) K−Mt, and (c) Ca−Mt. The stick framework represents the montmorillonite layer.

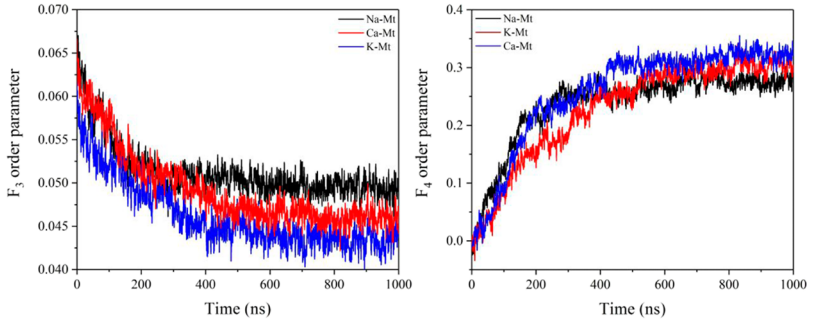

Figure 2. Evolution of order parameters in the different simulation models for run 3.

phase separation.[42,43] Then, the bulk solution model was added onto the montmorillonite sheet. Three models with different cations were abbreviated as Na−Mt, K−Mt, and Ca−Mt. Simulation for the different models were repeated at three times independently, which were recorded as run 1, run 2, and run 3, respectively. The initial configuration of the simulation model is illustrated in Figure 1.

Force Field and Simulation Details. All the MD simulations were performed with the GROMACS package (version 5.1.2).[44] Montmorillonite was modeled by the ClayFF force field.[45] The optimized potentials for liquid simulations all-atom force field was used for CH_4 molecules.[46] The TIP4P-Ice model was used for H_2O, and the settle algorithm was employed to constrain the rigid geometry of H_2O molecules.[47] The equation of motion was integrated with the leapfrog algorithm and with a time step of 1.0 fs. Lorentz−Berthelot combining rules were applied to calculate the Lennard-Jones potentials between different atoms. Short-range nonbonded interactions were cutoff at 1.25 nm.[48] The particle-mesh Ewald method was used to calculate the long-range electrostatic interactions with a Fourier spacing of 0.12 nm.[49]

In each MD simulation, energy minimization was performed to relax the initial configuration with the steepest descent algorithm at first. After energy minimization, 0.2 ns of isothermal−isobaric (NpT) ensemble simulation was employed for equilibration under 250 K and 50 MPa; the Berendsen coupling method was used to control temperature and pressure with a time constant of 0.1, and 0.5 ps, respectively. Subsequently, the equilibrated configuration was simulated in the NpT ensemble at the same temperature and pressure for 1000 ns, but temperature was controlled using the Nosé−Hoover thermostat[50] with a time constant of 1 ps, and pressure was controlled using the Parrinello−Rahman barostat[51] with a time constant of 4 ps. This temperature and pressure can provide sufficient driving force for attaining faster growth kinetics of CH_4 hydrate during the simulation.[43,52,53] Only the z dimension was scaled in NpT simulations. Periodic boundary conditions were imposed on the molecular structures in three directions.[54]

Data Analysis. *Order Parameter.* The tetrahedral order parameter (F_3)[55] and four-body order parameter (F_4)[56,57] were used to analyze the H_2O structure, and these were defined as follows (eqs 1 and 2)

$$F_3 = \left\langle \sum_{j=1}^{n_i-1} \sum_{k=j+1}^{n_i} (|\cos\theta_{jik}|\cos\theta_{jik} + \cos^2(109.47°))^2 \right\rangle \quad (1)$$

where θ_{jik} denotes the angle between the specified oxygen ith atom and the other two oxygen jth and kth atoms within a distance of 0.35 nm around the ith atom; n_i denotes the number of oxygen atoms. Average $\langle\ \rangle$ is computed over all H_2O molecules. The average values of the F_3 parameter remain at approximately 0.1 for liquid H_2O and 0.01 for solid H_2O (including CH_4 hydrate and ice).

$$F_4 = \frac{1}{n}\sum_{i=1}^{n} \cos 3\phi_i \quad (2)$$

where ϕ_i denotes the dihedral angle between the oxygen atoms of two adjacent molecules and the outermost hydrogen atoms, and n indicates the number of the oxygen atom pairs of H_2O molecules within 0.35 nm. The average values of F_4 are −0.04, −0.4, and 0.7 for H_2O, ice, and CH_4 hydrate, respectively.

Cage Structure. The structure of H_2O was identified by searching for oxygen atoms within 0.61 nm around CH_4 molecules. The topological structure of the ring formation was determined by the connection of the H_2O molecules. Two oxygen atoms were deemed connected if their distance was less than 0.35 nm. Then, all the possible pentagonal and hexagonal ring formations were identified via connected oxygen atoms. Oxygen atoms were utilized as the vertices to identify the 5^{12}, $5^{12}6^2$, $5^{12}6^3$, and $5^{12}6^4$ cages composed of 20, 24, 26, and 28H_2O molecules, respectively.[43,58,59]

https://dx.doi.org/10.1021/acsearthspacechem.9b00323
ACS Earth Space Chem. 2020, 4, 572−582

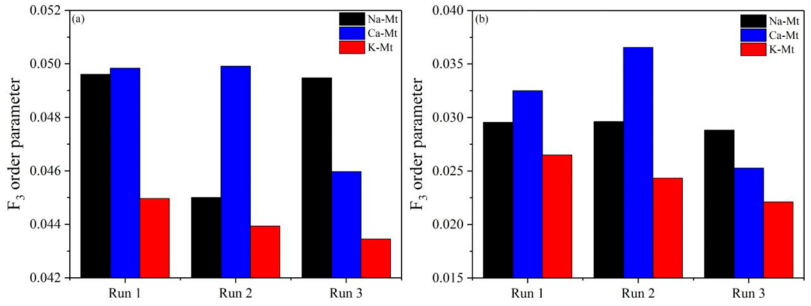

Figure 3. Average value of the F_3 order parameter in different simulation models during 800−1000 ns for run 1−3. (a) All H_2O molecules. (b) H_2O molecules in the bulk-like region.

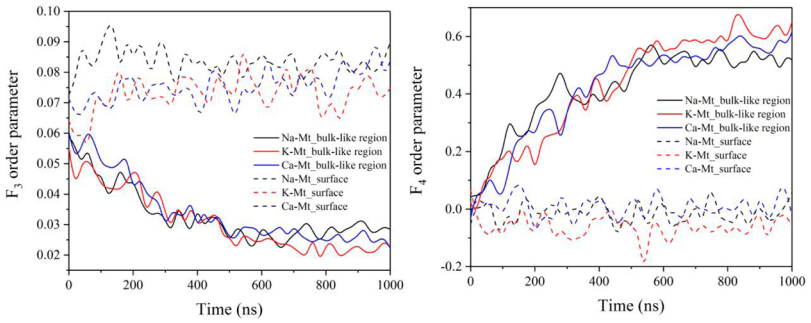

Figure 4. Evolution of order parameters for run 3 at the montmorillonite surface and the bulk-like region in different simulation models.

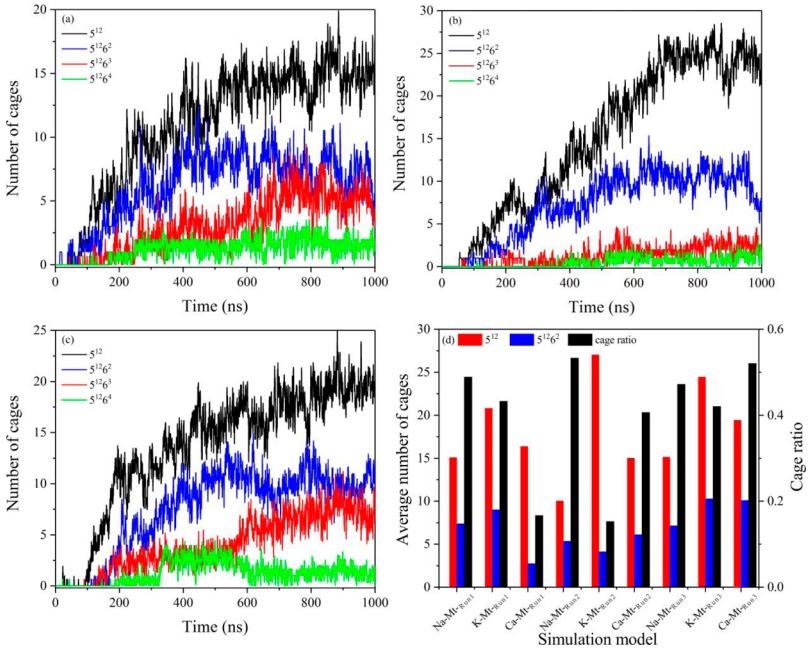

Figure 5. Evolution of the number of cages in different simulation models for run 3. (a) Na−Mt. (b) K−Mt. (c) Ca−Mt. (d) Number of 5^{12} and $5^{12}6^2$ cages averaged over the last 50 ns. The cage ratio of the average number of $5^{12}6^2$ to 5^{12} cages is also shown.

RESULTS AND DISCUSSION

Order Parameter and Cage Structural Analysis. The order parameter and cage structure were investigated to study the nucleation and growth events of CH_4 hydrate. Figure 2 shows the evolution of order parameters (F_3 and F_4) in different simulation models for run 3 (when averaged over all H_2O molecules). The plots of order parameters of all H_2O molecules in different simulation models for run 1 and run 2 are shown in Figure S1.

As shown in Figures 2 and S1, the decrease in F_3 and the increase in F_4 indicated the nucleation and growth process of the CH_4 hydrate, and the trend in order parameters demonstrated the transformation from a disordered state (liquid H_2O) to an ordered state (CH_4 hydrate). Compared with the F_3 and F_4 for different simulation models, the sharp changes in F_3 and F_4 indicated the rapid growth of CH_4 hydrate during 200−600 ns. After 600 ns, either F_4 or F_3 reached a steady value, which indicated that the growth of CH_4 hydrate almost finished, and a large number of CH_4 hydrate

https://dx.doi.org/10.1021/acsearthspacechem.9b00323
ACS Earth Space Chem. 2020, 4, 572−582

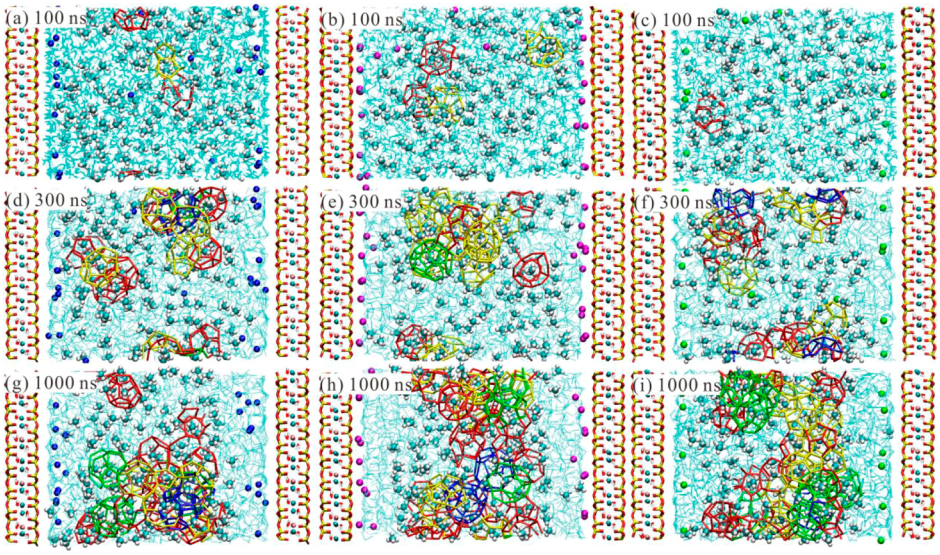

Figure 6. Snapshots of the CH_4 hydrate cages at different times in different simulation models for run 3. (a,d,g) Na−Mt. (b,e,h) K−Mt. (c,f,i) Ca−Mt. CH_4 hydrate cages are shown with different colors: red for 5^{12}, yellow for $5^{12}6^2$, green for $5^{12}6^3$, and blue for $5^{12}6^4$.

cages formed. The equilibrium values of F_3 and F_4 are between that of liquid H_2O and CH_4 hydrate, reflecting part of liquid H_2O was also present. It was expected that H_2O molecules cannot be completely converted into CH_4 hydrate because the CH_4/H_2O ratio was approximately 0.08 in this study. Additionally, the nucleation and subsequent growth of CH_4 hydrate results in a significant drop in potential energy during the simulation (Figure S2). The average values of the F_3 order parameter in different simulation models during 800−1000 ns for run 1−3 are shown in Figure 3a. There was little difference in the equilibrium values of F_3 in different montmorillonite models after CH_4 hydrate formation. The lower value of F_3 in the K−Mt model indicated that a more optimal tetrahedral structure of H_2O molecules was formed.

To analyze the effect of the external surface of montmorillonite on CH_4 hydrate formation, the evolution of both parameters in the bulk-like region (3.25−3.75 nm) and surface (the first adsorbed H_2O layer, <1.27 nm) was also investigated (Figures 4 and S3). In Figures 4 and S3, the value of F_4 and F_3 of H_2O molecules in the bulk-like region approached the value of the hydrate phase, which indicated that hydrate cages were formed beyond the montmorillonite surface. F_3 and F_4 of H_2O molecules on the montmorillonite surface approached the values of liquid H_2O, which might be because of the influence of cation hydration on the HB networks of H_2O structures, resulting in the liquid arrangement of H_2O molecules. Compared with Na−Mt and Ca−Mt, the lower F_3 value of H_2O molecules in the bulk-like region of the K−Mt model signified that it was favorable to form the optimal tetrahedral structure of H_2O molecules in K−Mt (Figure 3b). Therefore, the surface of K−Mt facilitated the nucleation of CH_4 hydrate in the bulk-like region, while the surface and the bulk-like region of Ca−Mt and Na−Mt did not show obvious promotion of CH_4 hydrate nucleation. In general, the surface of the K−Mt model could significantly promote the nucleation of CH_4 hydrate in the bulk-like solution. The bulk-like region in K−Mt was easier to form CH_4 hydrate cages than that in the Ca−Mt and Na−Mt.

To quantitatively disclose the evolution of hydrate cages during CH_4 hydrate formation, four different types of cage structures (*i.e.*, 5^{12}, $5^{12}6^2$, $5^{12}6^3$, and $5^{12}6^4$) were identified by using the cage analysis algorithm. Figures 5 and S4 show the evolution of cage structures in different simulation models during the simulation. The snapshot of cage structures at different simulation times shows the stages of nucleation and growth of CH_4 hydrate, which are shown in Figures 6 and S5. Figures 5 and S4 show that 5^{12} cages were first formed in the bulk-like solution, and the nucleation time (when the first stable cage structure formed) was different in different montmorillonite models, which was consistent with previous work that indicated that the nucleation process of hydrate tends to be more stochastic in terms of cage type and nucleation time.[60−63] The appearance of hydrate cages in the bulk-like region of the model was attributed to the locally high concentration of CH_4 molecules.[64] It was observed that the $5^{12}6^2$, $5^{12}6^3$, and $5^{12}6^4$ cages gradually appeared with increasing simulation time. The formation rates of the 5^{12} and $5^{12}6^2$ cages were higher than those of the $5^{12}6^3$ and $5^{12}6^4$ cages, which indicated that the formation of the 5^{12} and $5^{12}6^2$ cages was strongly correlated during the simulation. A small number of $5^{12}6^4$ cages in these models implied that it was difficult for CH_4 molecules to effectively stabilize the $5^{12}6^4$ cages because of the molecular size of the CH_4 molecule.[52] After CH_4 hydrate formation in different models, an amorphous crystal was finally obtained (Figure 6). Both structure I (sI) (5^{12} and $5^{12}6^2$ cages) and structure II (sII) (5^{12} and $5^{12}6^4$ cages) geometries were observed. The number of sI structures increased much faster than the number of sII structures with the CH_4 hydrate growth. Consequently, it can be said that the sI hydrate predominates. This result was in agreement with the fact that CH_4 can form only sI hydrate in nature.[1] Particularly, the number of 5^{12} cages in K−Mt was more than that in Ca−Mt and Na−Mt at the equilibrium stage. It was because of the hydration structure of cations in different models, leading to difference in CH_4 hydrate formation. The cage ratio is defined as the ratio of $5^{12}6^2$ cages with respect to 5^{12} cages. The cage ratio in different simulation models from 0.2 to 0.6 was significantly lower than the CH_4 hydrate structure (cage ration = 3).[65] Additionally, the ratios were also consistent with the

https://dx.doi.org/10.1021/acsearthspacechem.9b00323
ACS Earth Space Chem. 2020, 4, 572−582

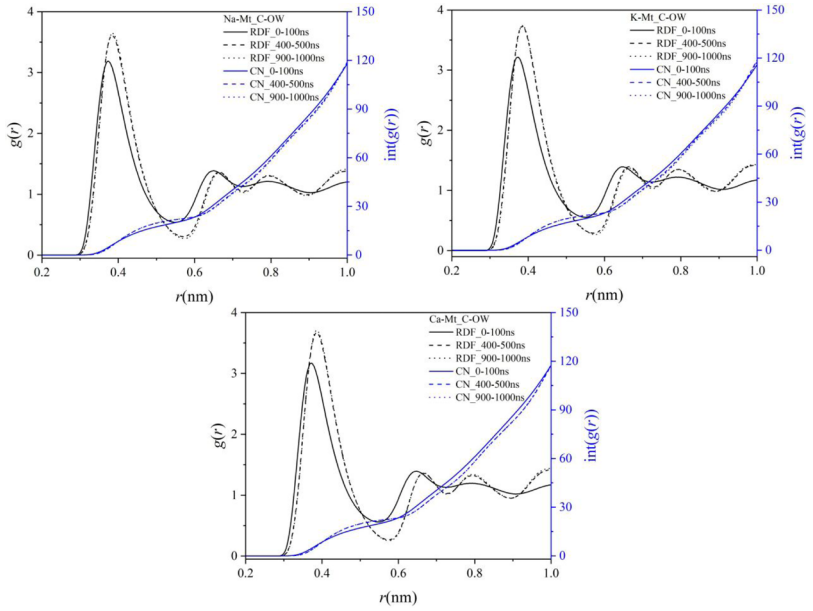

Figure 7. RDF of the OW around the C in different simulation models for run 3. OW and C represents the oxygen atom of H_2O and carbon atom of CH_4, respectively.

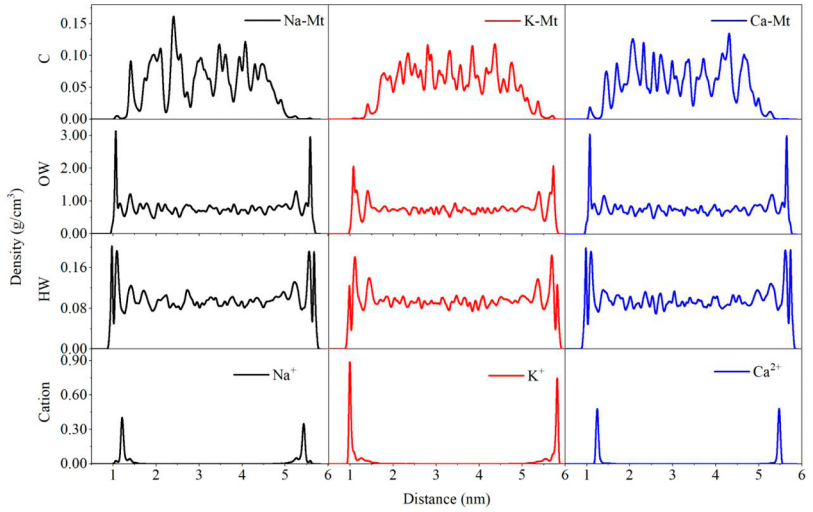

Figure 8. Density profile of different components along z direction for run 3. HW represents the hydrogen atom of H_2O.

previously reported model that the cations of montmorillonite affect the occupancy inside small cages of CH_4 hydrate.[66]

Moreover, CH_4 hydrate formation was further supported by the RDF and coordination number (CN) of the oxygen atom (OW) in H_2O and around carbon atom (C) in the CH_4. The RDF for component B around A is defined as $g_{A-B}(r) = \frac{dN_{A-B}}{dr}\frac{1}{4\pi\rho_B r^2}$, where ρ_B is the average density of component B, dN_{A-B} is the average number of component B around A between the region of r and $r + dr$, and CN of B around A was obtained from the integral of the RDF profile from the position starting at $r = 0$ to the position of the first minimum located after the first peak.[48] In Figure 7, the first peak of $g_{C-OW}(r)$ appeared at approximately 0.386 nm and was in good agreement with the neutron diffraction results and pair correlation functions for CH_4 hydrate.[67] The CNs of H_2O molecules around the CH_4 in the Na−Mt, K−Mt, and Ca−Mt models were 22.50, 22.53, and 22.63, respectively. These results were in good agreement with those of the fully formed CH_4 hydrate in previous work.[67] In addition, Figure S6 illustrates the RDFs of C−C and OW−OW during three segments of simulation trajectories (0−100, 400−500, and 900−1000 ns). A strong peak of $g_{C-C}(r)$ occurred at approximately 0.384 nm during 0−100 ns, which indicated that the CH_4 molecules were distributed in contact with each other in the liquid phase. Then, the peak at 0.384 nm almost disappeared, and a strong peak merged at approximately 0.648 nm during 900−1000 ns, which was consistent with the distance between CH_4 molecules in the bulk CH_4 hydrate phase.[68,69] The third peak appeared at approximately 1.05 nm, but it also exhibited a small and broad peak at 0.39 nm. All the results demonstrated that CH_4−CH_4 molecular interactions occurred across the hydrate structures during the CH_4 hydrate formation. The $g_{OW-OW}(r)$ function is defined as the oxygen−oxygen distance between two H_2O molecules. Among all montmorillonite models, the first, second, and third peaks of $g_{OW-OW}(r)$ appeared at approximately 0.28, 0.45, and 0.65 nm,

https://dx.doi.org/10.1021/acsearthspacechem.9b00323
ACS Earth Space Chem. 2020, 4, 572−582

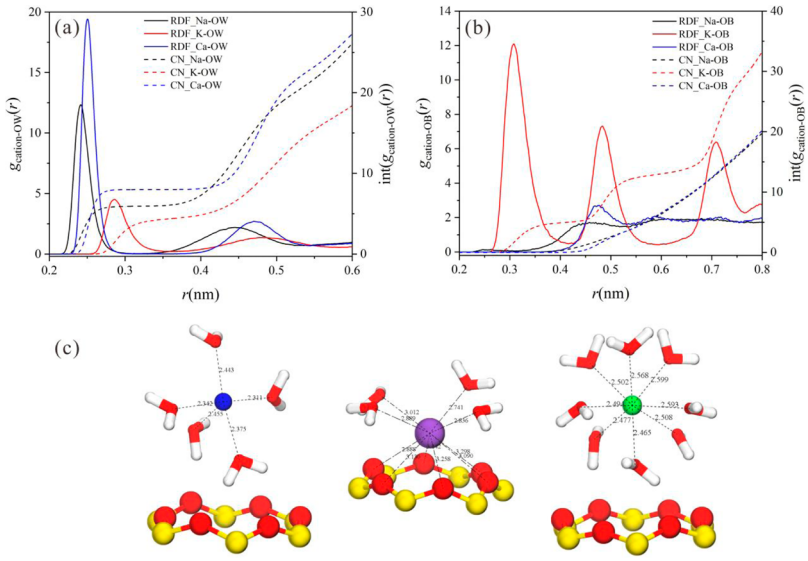

Figure 9. RDF of cation−OW (a) and cation−OB (b) in different simulation models for run 3. (c) From left to right: hydration structure of Na^+, K^+, and Ca^{2+} cations, respectively. Na^+, K^+, and Ca^{2+} are shown as blue ball, violet ball, and green ball, respectively.

respectively. This result was consistent with that of stable bulk CH_4 hydrate,[68] indicating that the H_2O molecules were arranged in clathrate-like structures.

Density Profile of Different Components. To investigate the interaction of cations, CH_4, and H_2O molecules with the montmorillonite surface, the distributions of different components, perpendicular to the montmorillonite sheets, were calculated. The snapshot of cation distribution in different simulation models is shown in Figure S7. The density profile of different components is shown in Figure 8.

The density profile was averaged over the simulation trajectory from 600 to 1000 ns. In Figure 8, a large amount of CH_4 molecules was distributed in the bulk-like region. The H_2O distribution was symmetric with two peaks on both sides. OW of the first-adsorbed H_2O layer was located at distances of 0.94−1.26, 0.96−1.28, and 0.94−1.27 nm above the Na−Mt, K−Mt, and Ca−Mt surfaces, respectively. HW of the first adsorbed H_2O layer was located at distances of 0.87−1.01, 0.88−1.03, and 0.87−1.03 nm above the Na−Mt, K−Mt, and Ca−Mt surfaces, respectively. The position of OW and HW demonstrated the orientation of H_2O molecules in the first adsorbed H_2O layer. The density of the adsorbed H_2O layer in Na−Mt and Ca−Mt was approximately 3.0 g/cm^3, while that in K−Mt was approximately 2.0 g/cm^3. The subtle differences in H_2O density were attributed to the adsorption behavior of cations on the montmorillonite surface. The Na^+, K^+, and Ca^{2+} were mainly located at distances of 1.11−1.32, 0.92−1.17, and 1.17−1.4 nm, respectively. The K^+ was distributed closer to the surface than Na^+ and Ca^{2+}. Na^+ and Ca^{2+} were distributed predominantly in the outer sphere. However, K^+ was distributed in the vacancies of the hexagonal rings of the Si−O tetrahedron, where they formed an inner-sphere adsorption, and the basal oxygen atoms (OB) also contributed to their first hydration shell (Figure 9).

The hydration characteristics of Na^+, K^+, and Ca^{2+} were consistent with the findings of previous research.[70,71] Figure 9a,b provides the RDFs of $g_{\text{cation-OW}}(r)$ and $g_{\text{cation-OB}}(r)$ during the last 10 ns. The first peak of $g_{\text{cation-OW}}(r)$ in Na−Mt, K−Mt, and Ca−Mt appeared at approximately 0.242, 0.288, and 0.25 nm, respectively, (Figure 9a), which represents the hydration radii of Na^+, K^+, and Ca^{2+}, respectively. The intensity of the first peak and the hydration radius of different cations in the $g_{\text{cation-ow}}(r)$ curves indicated the different hydration abilities and hydration enthalpies of these cations, which were consistent with previous results.[72] However, as for the distribution of K^+ on the montmorillonite surface, part of the oxygen coordination was provided by the OB, where the first peak of $g_{\text{cation-OB}}(r)$ in K−Mt appeared at approximately 0.31 nm (Figure 9b). The CN of OB around the K^+ was approximately 5.034, while the contribution of OB was close to zero for Na^+ and Ca^{2+}. Note that the total CNs of Na^+, K^+, and Ca^{2+} were 5.928, 9.529, and 7.993, respectively. In general, the cation hydration on the montmorillonite surface alters the number of H_2O molecules involved in the CH_4 hydrate formation. Additionally, the number of CH_4 molecules decreased near the montmorillonite surface because of the salting-out effect, which reduced the solubility of CH_4 molecules in the solution caused by Na^+ hydration and increased the propensity of CH_4 molecules to be adsorbed on the hydrate surface.[73,74] The $g_{\text{cation-C}}(r)$ also supported this result from Figure S8, which shows that the intensity of RDF peaks for CH_4 around Na^+, K^+, and Ca^{2+} decreased during CH_4 hydrate formation. The cations near the montmorillonite surface would disrupt the HB structures of interfacial H_2O molecules, which might affect the hydrate formation in the bulk-like region. Thus, the effect of the external surface of montmorillonite on CH_4 hydrate formation depends on the hydration properties of different surface cations.

Hydrogen Bond Structural Analysis. The H_2O molecules in the CH_4 hydrate are connected by HBs. The HB networks are frequently formed and broken during CH_4 hydrate formation. It is important to assess the number and length of the HB structure at different regions of the simulation models during CH_4 hydrate formation. The first strong peaks of $g_{\text{OB-HW}}(r)$ and $g_{\text{OW-HW}}(r)$ both appeared at approximately 0.184 nm (Figure S9), which was close to the HB distance of H_2O molecules in hydrate cages. From Figure S10a,b, the average number of HBs in the Na−Mt and Ca−Mt models was almost identical. The average number of HBs per H_2O molecule and the average number of HBs per H_2O molecule

https://dx.doi.org/10.1021/acsearthspacechem.9b00323
ACS Earth Space Chem. 2020, 4, 572−582

contributing to other H_2O molecules in K−Mt model were apparently greater than that of the Na−Mt and Ca−Mt models, which implied that the arrangement of H_2O molecules in the K−Mt model was more regular than that in the Ca−Mt and Na−Mt models. Hence, these results demonstrated that the average number of HBs per H_2O molecule in the models was approximate to the number in the bulk solid H_2O phase,[75,76] illustrating the formation of the hydrate phase. As expected, because of the inner-sphere adsorption behavior of K^+ cations on the montmorillonite surface, the average number of HBs per H_2O molecule contributing to the Si−O tetrahedral in K−Mt was slightly lower than that of the Na−Mt and Ca−Mt models (Figure S10c). Therefore, compared with the Na−Mt and Ca−Mt models, a small number of H_2O molecules was involved in the formation of HBs on the K−Mt surface.

Diffusion Coefficient of H_2O Molecules. To access the reliability of the diffusion properties of H_2O molecules during CH_4 hydrate formation, the self-diffusion coefficient D of different components was calculated as follows: $\frac{1}{N}\sum_{i=1}^{N}\langle|\vec{r}_i(t) - \vec{r}_i(0)|^2\rangle = 2dtD$, where N denotes the number of atoms of the selected components, $\vec{r}_i(t)$ denotes the center-of-mass position of the ith atom at time t, and d indicates the diffusion dimension (*i.e.*, $d = 3$ for the total self-diffusion coefficient). The left-hand side is usually termed as the MSD.[48,77] Figure S11 illustrates the MSD profile of H_2O molecules in different simulation models during the last 10 ns for run 3. The MSD profiles of H_2O molecules were fitted for calculating the self-diffusion coefficients, which are 0.96×10^{-7} cm^2/s for Na−Mt, 1.33×10^{-7} cm^2/s for K−Mt, and 0.98×10^{-7} cm^2/s for Ca−Mt. Therefore, the self-diffusion of H_2O molecules in Na−Mt and Ca−Mt was basically identical and less than that in K−Mt. The possible reasons for this result are as follows. On the one hand, the formation of hydrate decreases the diffusion coefficient of H_2O molecules. On the other hand, the presence of cations on the external surface of montmorillonite leads to the difference in the cage number, resulting in the different diffusion coefficients of H_2O molecules. Third, the coordination structure of cations could also restrict the diffusion of H_2O molecules.

The abovementioned simulation results show that the CH_4 hydrate formation differs in the montmorillonite with different surface cations because of the effects of the coordination structure of cations. The balance between cation/surface, cation/H_2O, and H_2O/surface interactions controlled the structural complexes on the montmorillonite surface. The size and the charge amount of cations on the surface significantly influenced the CH_4 hydrate formation by altering the cage occupancy of CH_4 hydrate. In the nucleation stage, the hydrate cages were formed in the bulk-like solution because of the local high CH_4 concentration. The hydrate nucleus grew in the bulk-like solution, and the number of HBs per H_2O molecules gradually increased. During the growth stage, the population of sI structures increased much faster than that of the sII structures. This result suggests that the nucleus of CH_4 hydrate in montmorillonite models mainly grows into an sI crystal, which was in accordance with the fact that CH_4 molecules can only form sI hydrate. In addition, the number of 5^{12} cages in K−Mt was more than that in Ca−Mt and Na−Mt, resulting in different types of hydrate formation on the external surface of montmorillonite with different cations.

In natural gas hydrate-bearing sediment environments, the content and surface cations of montmorillonite vary for different sedimentary basins.[18,19,35] Generally speaking, the pore H_2O in the sediment contains Na^+, K^+, Ca^{2+}, Cl^-, and SO_4^{2-} ions, which originated from the ocean H_2O deep brine.[78] Such pore H_2O resulted from the mixing of seawater with the fluids released from the dehydration and illitization reactions involving smectite in-depth.[35] The cations in pore H_2O readily exchange with cations from the montmorillonite surface or are attracted by the defects on the surface, generating montmorillonite with different surface cations. The present work shows that the hydration of cations affected the formation and distribution of CH_4 hydrate beyond the montmorillonite surface. The aqueous environment dominated by K^+ on the external surface of montmorillonite facilitate heterogeneous nucleation of CH4 hydrate rather than that by Ca^{2+} or Na^+. The findings implied that the effect of surface cations of montmorillonite on CH_4 hydrate formation should be considered in montmorillonite-rich sedimentary basins. Therefore, the natural gas hydrate reservoir with a higher montmorillonite content might effectively inhibit secondary hydrate formation during CH_4 production and thus should be considered for such results in natural gas hydrate development.

Furthermore, the ability of the inhibition effect of montmorillonite on CH_4 hydrate formation has significant implications for the formation of hydrate plugs in the wellbore during deepwater drilling. Two major problems with CH_4 hydrate are generated in deepwater drilling with H_2O-based drilling muds.[25] On the one hand, the hydrate may form a plug in the wellbore to prevent drill string rotation because of the mechanical strength of a large mass of hydrates. On the other hand, the loss of a large number of H_2O molecules from the drilling mud severely influences the mud fluidity. In the most extreme scenario, all solid particles will settle out in the wellbore. Therefore, it is hoped that montmorillonite could effectively prevent CH_4 hydrate formation in deepwater drilling.

■ CONCLUSIONS

MD simulation was performed to examine the formation process of CH_4 hydrate with different cations (Na^+, K^+, and Ca^{2+}) located on the external surface of montmorillonite. According to the results obtained, the nucleus grows in the bulk-like solution to form 5^{12}, $5^{12}6^2$, $5^{12}6^3$, and $5^{12}6^4$ cages. The number of sI structures increased faster than that of the sII structure. The cations exhibited a monolayer adsorption configuration with inner-sphere (K^+) and outer-sphere (Na^+ and Ca^{2+}) hydration behavior on the montmorillonite surface, resulting in different coordination structures with surface cations. As a result, CH_4 molecules cannot break through the hydration layer to form CH_4 hydrate near the surface. The arrangement of H_2O molecules in K−Mt exhibited a more optimal tetrahedral structure than that in the Ca−Mt and Na−Mt surface, indicating that the K−Mt surface could facilitate the nucleation of CH_4 hydrate in the bulk-like solution as compared to that of the Ca−Mt and Na−Mt surfaces. Additionally, the number of 5^{12} cages decreased in the order: Na−Mt < Ca−Mt < K−Mt. Therefore, this study notes that the existence of cations on the surface of montmorillonite plays a key role in controlling CH_4 hydrate formation through altering the cage occupancy of the CH_4 hydrate. These findings are significant not only for understanding the formation mechanism of CH_4 hydrate in natural sediments with abundant montmorillonite but also for its potential application in

https://dx.doi.org/10.1021/acsearthspacechem.9b00323
ACS Earth Space Chem. 2020, 4, 572−582

inhibiting the CH_4 hydrate formation in deepwater drilling and natural gas hydrate development.

■ ASSOCIATED CONTENT

Supporting Information

The Supporting Information is available free of charge at https://pubs.acs.org/doi/10.1021/acsearthspacechem.9b00323.

Evolution of order parameters in different models for run 1-2, potential energy in different models for run 3, evolution of order parameters at the montmorillonite surface and the bulk-like region in different models for run 1-2, and the number of cages in different models for run 1-2, snapshots of CH_4 hydrate cages in different models for run 1-2 at 1000 ns, RDF of C-C and C-OW, snapshot of cation distribution along the x-y plane in different models for run 3, RDF of cation-C, OW-HW and OB-HW in different models for run 3, number of HBs for run 3, and MSD of H_2O molecules in different models for run 3 (PDF)

■ AUTHOR INFORMATION

Corresponding Author

Peng Yuan − *CAS Key Laboratory of Mineralogy and Metallogeny, Guangdong Provincial Key Laboratory of Mineral Physics and Materials, Guangzhou Institute of Geochemistry, Institutions of Earth Science, Chinese Academy of Sciences (CAS), Guangzhou 510640, China;* orcid.org/0000-0001-6492-0509; Phone: +86 20 85290341; Email: yuanpeng@gig.ac.cn

Authors

Yun Li − *CAS Key Laboratory of Mineralogy and Metallogeny, Guangdong Provincial Key Laboratory of Mineral Physics and Materials, Guangzhou Institute of Geochemistry, Institutions of Earth Science, Chinese Academy of Sciences (CAS), Guangzhou 510640, China; University of Chinese Academy of Sciences, Beijing 100049, China*

Meng Chen − *CAS Key Laboratory of Mineralogy and Metallogeny, Guangdong Provincial Key Laboratory of Mineral Physics and Materials, Guangzhou Institute of Geochemistry, Institutions of Earth Science, Chinese Academy of Sciences (CAS), Guangzhou 510640, China;* orcid.org/0000-0002-1878-2261

Hongzhe Song − *CAS Key Laboratory of Mineralogy and Metallogeny, Guangdong Provincial Key Laboratory of Mineral Physics and Materials, Guangzhou Institute of Geochemistry, Institutions of Earth Science, Chinese Academy of Sciences (CAS), Guangzhou 510640, China; University of Chinese Academy of Sciences, Beijing 100049, China*

Baifa Zhang − *CAS Key Laboratory of Mineralogy and Metallogeny, Guangdong Provincial Key Laboratory of Mineral Physics and Materials, Guangzhou Institute of Geochemistry, Institutions of Earth Science, Chinese Academy of Sciences (CAS), Guangzhou 510640, China; University of Chinese Academy of Sciences, Beijing 100049, China*

Dong Liu − *CAS Key Laboratory of Mineralogy and Metallogeny, Guangdong Provincial Key Laboratory of Mineral Physics and Materials, Guangzhou Institute of Geochemistry, Institutions of Earth Science, Chinese Academy of Sciences (CAS), Guangzhou 510640, China*

Huijun Zhou − *CAS Key Laboratory of Mineralogy and Metallogeny, Guangdong Provincial Key Laboratory of Mineral Physics and Materials, Guangzhou Institute of Geochemistry, Institutions of Earth Science, Chinese Academy of Sciences (CAS), Guangzhou 510640, China; University of Chinese Academy of Sciences, Beijing 100049, China*

Hongling Bu − *CAS Key Laboratory of Mineralogy and Metallogeny, Guangdong Provincial Key Laboratory of Mineral Physics and Materials, Guangzhou Institute of Geochemistry, Institutions of Earth Science, Chinese Academy of Sciences (CAS), Guangzhou 510640, China*

Complete contact information is available at: https://pubs.acs.org/10.1021/acsearthspacechem.9b00323

Notes

The authors declare no competing financial interest.

■ ACKNOWLEDGMENTS

This work was supported by National Special Support for High-Level Personnel and Youth Innovation Promotion Association CAS for the excellent members (2016-81-01), National Natural Science Foundation of China (grant nos. 41472044, 41272059, and 41602034). This is a contribution (no. IS-2841) from GIGCAS.

■ REFERENCES

(1) Sloan, E. D.; Carolyn, A. K. *Clathrate Hydrates of Natural Gases*, 3rd ed.; Taylor & Francis, 2007; pp 60−61.

(2) Jager, M. D.; Sloan, E. D. The effect of pressure on methane hydration in pure water and sodium chloride solutions. *Fluid Phase Equil.* **2001**, *185*, 89−99.

(3) Sun, R.; Duan, Z. An accurate model to predict the thermodynamic stability of methane hydrate and methane solubility in marine environments. *Chem. Geol.* **2007**, *244*, 248−262.

(4) Sloan, E. D. Physical/chemical properties of gas hydrates and application to world margin stability and climatic change. *J. Vac. Sci. Technol.* **1998**, *137*, 31−50.

(5) Warrier, P.; Khan, M. N.; Srivastava, V.; Maupin, C. M.; Koh, C. A. Overview: Nucleation of clathrate hydrates. *J. Chem. Phys.* **2016**, *145*, 211705.

(6) Cygan, R. T.; Guggenheim, S.; Koster van Groos, A. F. Molecular models for the intercalation of methane hydrate complexes in montmorillonite clay. *J. Phys. Chem. B* **2004**, *108*, 15141−15149.

(7) Saw, V. K.; Udayabhanu, G. N.; Mandal, A.; Laik, S. Methane Hydrate Formation and Dissociation in the presence of Bentonite Clay Suspension. *Chem. Eng. Technol.* **2013**, *36*, 810−818.

(8) Uchida, T.; Takeya, S.; Chuvilin, E. M.; Ohmura, R.; Nagao, J.; Yakushev, V. S.; Istomin, V. A.; Minagawa, H.; Ebinuma, T.; Narita, H. Decomposition of methane hydrates in sand, sandstone, clays, and glass beads. *J. Geophys. Res.: Solid Earth* **2004**, *109*, B05206.

(9) Lamorena, R. B.; Lee, W. Formation of carbon dioxide hydrate in soil and soil mineral suspensions with electrolytes. *Environ. Sci. Technol.* **2008**, *42*, 2753−2759.

(10) Seo, Y.-j.; Sun-Hwa, Y. Structural, Mineralogical, and Rheological Properties of Methane Hydrates in Smectite Clays. *J. Chem. Eng. Data* **2009**, *54*, 1284−1291.

(11) Yeon, S.-H.; Seol, J.; Seo, Y.-j.; Park, Y.; Koh, D.-Y.; Park, K.-P.; Huh, D.-G.; Lee, J.; Lee, H. Effect of interlayer ions on methane hydrate formation in clay sediments. *J. Phys. Chem. B* **2009**, *113*, 1245−1248.

(12) Choudhary, N.; Hande, V. R.; Roy, S.; Chakrabarty, S.; Kumar, R. Effect of Sodium Dodecyl Sulfate Surfactant on Methane Hydrate Formation: A Molecular Dynamics Study. *J. Phys. Chem. B* **2018**, *122*, 6536−6542.

(13) Veluswamy, H. P.; Lee, P. Y.; Premasinghe, K.; Linga, P. Effect of Biofriendly Amino Acids on the Kinetics of Methane Hydrate

Formation and Dissociation. *Ind. Eng. Chem. Res.* **2017**, *56*, 6145−6154.
(14) Sa, J.-H.; Kwak, G. H.; Han, K.; Ahn, D.; Cho, S. J.; Ju, D. L.; Lee, H. Inhibition of methane and natural gas hydrate formation by altering the structure of water with amino acids. *Sci. Rep.* **2016**, *6*, 31582.
(15) Wu, G.; Ji, H.; Tian, L.; Chen, D. Effects of Salt Ions on the Methane Hydrate Formation and Dissociation in the Clay Pore Water and Bulk Water. *Energy Fuels* **2018**, *32*, 12486−12494.
(16) Kim, D.; Ahn, Y.-H.; Kim, S.-J.; Lee, J. Y.; Lee, J.; Seo, Y.-j.; Lee, H. Gas Hydrate in Crystalline-Swelled Clay: The Effect of Pore Dimension on Hydrate Formation and Phase Equilibria. *J. Phys. Chem. C* **2015**, *119*, 22148−22153.
(17) Guggenheim, S.; van Groos, A. F. K. New gas-hydrate phase: Synthesis and stability of clay-methane hydrate intercalate. *Geology* **2003**, *31*, 653−656.
(18) Clennell, M. B.; Henry, P.; Hovland, M.; Booth, J. S.; Thomas, M. Formation of Natural Gas Hydrates in Marine Sediments: Gas Hydrate Growth and Stability Conditioned by Host Sediment Properties. *Ann. N.Y. Acad. Sci.* **1999**, *912*, 887−896.
(19) Martín-Puertas, C.; Mata, M. P.; Fernández-Puga, M. C.; Díaz del Río, V.; Vázquez, J. T.; Somoza, L. A comparative mineralogical study of gas-related sediments of the Gulf of Cádiz. *Geo Mar. Lett.* **2007**, *27*, 223−235.
(20) Cha, S. B.; Ouar, H.; Wildeman, T. R.; Sloan, E. D. A third-surface effect on hydrate formation. *J. Phys. Chem.* **1988**, *92*, 6492−6494.
(21) Zhou, Q.; Lu, X.; Liu, X.; Zhang, L.; He, H.; Zhu, J.; Yuan, P. Hydration of methane intercalated in Na-smectites with distinct layer charge: Insights from molecular simulations. *J. Colloid Interface Sci.* **2011**, *355*, 237−242.
(22) Bergaya, F.; Lagaly, G. *Handbook of Clay Science*; Developments of Clay Science; Elsevier: Amsterdam, 2013; Vol. *1*, pp 23−25.
(23) Liu, D.; Yuan, P.; Liu, H.; Cai, J.; Qin, Z.; Tan, D.; Zhou, Q.; He, H.; Zhu, J. Influence of heating on the solid acidity of montmorillonite: A combined study by DRIFT and Hammett indicators. *Appl. Clay Sci.* **2011**, *52*, 358−363.
(24) Park, S.-H.; Sposito, G. Do Montmorillonite Surfaces Promote Methane Hydrate Formation? Monte Carlo and Molecular Dynamics Simulations. *J. Phys. Chem. B* **2003**, *107*, 2281−2290.
(25) Kotkoskie, T. S.; Al-Ubaidi, B.; Wildeman, T. R.; Sloan, E. D. Inhibition of gas hydrates in water-based drilling muds. *SPE Drill. Eng.* **1992**, *7*, 130−136.
(26) Park, T.; Kyung, D.; Lee, W. Effect of organic matter on CO_2 hydrate phase equilibrium in phyllosilicate suspensions. *Environ. Sci. Technol.* **2014**, *48*, 6597−6603.
(27) Kim, D.; Lee, H. Phase behavior of gas hydrates in nanoporous materials: Review. *Korean J. Chem. Eng.* **2016**, *33*, 1977−1988.
(28) Chong, Z. R.; Chan, A. H. M.; Babu, P.; Yang, M.; Linga, P. Effect of NaCl on methane hydrate formation and dissociation in porous media. *J. Nat. Gas Sci. Eng.* **2015**, *27*, 178−189.
(29) Nguyen, N. N.; Nguyen, A. V. The dual effect of sodium halides on the formation of methane gas hydrate. *Fuel* **2015**, *156*, 87−95.
(30) Cha, M.; Hu, Y.; Sum, A. K. Methane hydrate phase equilibria for systems containing NaCl, KCl, and NH_4Cl. *Fluid Phase Equil.* **2016**, *413*, 2−9.
(31) Hensen, C.; Nuzzo, M.; Hornibrook, E.; Pinheiro, L. M.; Bock, B.; Magalhães, V. H.; Brückmann, W. Sources of mud volcano fluids in the Gulf of Cadiz-indications for hydrothermal imprint. *Geochim. Cosmochim. Acta* **2007**, *71*, 1232−1248.
(32) Sun, X.; Mohanty, K. K. Kinetic simulation of methane hydrate formation and dissociation in porous media. *Chem. Eng. Sci.* **2006**, *61*, 3476−3495.
(33) Wilder, J. W.; Seshadri, K.; Smith, D. H. Modeling Hydrate Formation in Media with Broad Pore Size Distributions. *Langmuir* **2001**, *17*, 6729−6735.
(34) Wang, H.; Chen, L.; Qu, Z.; Yin, Y.; Kang, Q.; Yu, B.; Tao, W.-Q. Modeling of multi-scale transport phenomena in shale gas production—a critical review. *Appl. Energy* **2020**, *262*, 114575.
(35) Wilder, J. W.; Seshadri, K.; Smith, D. H. Modeling Hydrate Formation in Media with Broad Pore Size Distributions. *Langmuir* **2001**, *17*, 6729−6735.
(36) Titiloye, J. O.; Skipper, N. T. Molecular dynamics simulation of methane in sodium montmorillonite clay hydrates at elevated pressures and temperatures. *Mol. Phys.* **2001**, *99*, 899−906.
(37) Lee, J. H.; Guggenheim, S. Single crystal X-ray refinement of pyrophyllite-1 Tc. *Am. Mineral.* **1981**, *66*, 350−357.
(38) Downs, R. T.; Hall-Wallace, M. The American Mineralogist crystal structure database. *Am. Mineral.* **2003**, *88*, 247−250.
(39) Loewenstein, W. The distribution of aluminum in the tetrahedra of silicates and aluminates. *Am. Mineral.* **1954**, *39*, 92−96.
(40) Li, X.; Li, H.; Yang, G. Configuration, anion-specific effects, diffusion, and impact on counterions for adsorption of salt anions at the interfaces of clay minerals. *J. Phys. Chem. C* **2016**, *120*, 14621−14630.
(41) Zhang, L.; Lu, X.; Liu, X.; Yang, K.; Zhou, H. Surface wettability of basal surfaces of clay minerals: Insights from molecular dynamics simulation. *Energy Fuels* **2016**, *30*, 149−160.
(42) Bhattacharjee, G.; Choudhary, N.; Kumar, A.; Chakrabarty, S.; Kumar, R. Effect of the amino acid l -histidine on methane hydrate growth kinetics. *J. Nat. Gas Sci. Eng.* **2016**, *35*, 1453−1462.
(43) Jiménez-Ángeles, F.; Firoozabadi, A. Nucleation of methane hydrates at moderate subcooling by molecular dynamics simulations. *J. Phys. Chem. C* **2014**, *118*, 11310−11318.
(44) Hess, B.; Kutzner, C.; van der Spoel, D.; Lindahl, E. GROMACS 4: algorithms for Highly Efficient, Load-Balanced, and Scalable Molecular Simulation. *J. Chem. Theory Comput.* **2008**, *4*, 435−447.
(45) Cygan, R. T.; Liang, J.-J.; Kalinichev, A. G. Molecular Models of Hydroxide, Oxyhydroxide, and Clay Phases and the Development of a General Force Field. *J. Phys. Chem. B* **2004**, *108*, 1255−1266.
(46) Jorgensen, W. L.; Madura, J. D.; Swenson, C. J. Optimized intermolecular potential functions for liquid hydrocarbons. *J. Am. Chem. Soc.* **1984**, *106*, 6638−6646.
(47) Abascal, J. L. F.; Sanz, E.; Fernández, R.; García, V.. C. A potential model for the study of ices and amorphous water: TIP4P/Ice. *J. Chem. Phys.* **2005**, *122*, 234511.
(48) Allen, M. P.; Tildesley, D. J. *Computer Simulation of Liquids*; Oxford university press, 2017.
(49) Darden, T.; York, D.; Pedersen, L. Particle mesh Ewald: An N·log (N) method for Ewald sums in large systems. *J. Chem. Phys.* **1993**, *98*, 10089−10092.
(50) Evans, D. J.; Holian, B. L. The nose-hoover thermostat. *J. Chem. Phys.* **1985**, *83*, 4069−4074.
(51) Parrinello, M.; Rahman, A. Polymorphic transitions in single crystals: A new molecular dynamics method. *J. Appl. Phys.* **1981**, *52*, 7182−7190.
(52) Walsh, M. R.; Koh, C. A.; Sloan, E. D.; Sum, A. K.; Wu, D. T. Microsecond simulations of spontaneous methane hydrate nucleation and growth. *Science* **2009**, *326*, 1095−1098.
(53) Jenel, V.; Kusalik, P. G. Unusual crystalline and polycrystalline structures in methane hydrates. *J. Am. Chem. Soc.* **2006**, *128*, 15588−15589.
(54) Makov, G.; Payne, M. C. Periodic boundary conditions in ab initio calculations. *Phys. Rev. B* **1995**, *51*, 4014−4022.
(55) Báez, L. A.; Clancy, P. Computer Simulation of the Crystal Growth and Dissolution of Natural Gas Hydrates. *Ann. N.Y. Acad. Sci.* **1994**, *715*, 177−186.
(56) Rodger, P. M.; Forester, T. R.; Smith, W. Simulations of the methane hydrate/methane gas interface near hydrate forming conditions conditions. *Fluid Phase Equil.* **1996**, *116*, 326−332.
(57) Moon, C.; Hawtin, R. W.; Rodger, P. M. Nucleation and control of clathrate hydrates: insights from simulation. *Faraday Discuss.* **2007**, *136*, 367−382.
(58) Jiménez-Ángeles, F.; Firoozabadi, A. Enhanced hydrate nucleation near the limit of stability. *J. Phys. Chem. C* **2015**, *119*, 8798−8804.

https://dx.doi.org/10.1021/acsearthspacechem.9b00323
ACS Earth Space Chem. 2020, 4, 572−582

(59) Jacobson, L. C.; Hujo, W.; Molinero, V. Thermodynamic stability and growth of guest-free clathrate hydrates: a low-density crystal phase of water. *J. Phys. Chem. B* **2009**, *113*, 10298−10307.
(60) Ji, H.; Chen, D.; Chen, Z.; Wu, G. Molecular Dynamics Simulation of Methane Hydrate Formation and Dissociation in the Clay Pores With Fatty Acids. *J. Phys. Chem. C* **2018**, *122*, 1318−1325.
(61) Guo, G.-J.; Rodger, P. M. Solubility of aqueous methane under metastable conditions: implications for gas hydrate nucleation. *J. Phys. Chem. B* **2013**, *117*, 6498−6504.
(62) Walsh, M. R.; Beckham, G. T.; Koh, C. A.; Sloan, E. D.; Wu, D. T.; Sum, A. K. Methane hydrate nucleation rates from molecular dynamics simulations: Effects of aqueous methane concentration, interfacial curvature, and system size. *J. Phys. Chem. C* **2011**, *115*, 21241−21248.
(63) Zhang, Z.; Walsh, M. R.; Guo, G.-J. Microcanonical molecular simulations of methane hydrate nucleation and growth: Evidence that direct nucleation to sI hydrate is among the multiple nucleation pathways. *Phys. Chem. Chem. Phys.* **2015**, *17*, 8870−8876.
(64) Jacobson, L. C.; Hujo, W.; Molinero, V. Amorphous precursors in the nucleation of clathrate hydrates. *J. Am. Chem. Soc.* **2010**, *132*, 11806−11811.
(65) Sarupria, S.; Debenedetti, P. G. Homogeneous Nucleation of Methane Hydrate in Microsecond Molecular Dynamics Simulations. *J. Phys. Chem. Lett.* **2012**, *3*, 2942−2947.
(66) Yeon, S.-H.; Seol, J.; Koh, D.-Y.; Seo, Y.-j.; Park, K.-P.; Huh, D.-G.; Lee, J.; Lee, H. Abnormal methane occupancy of natural gas hydrates in deep sea floor sediments. *Energy Environ. Sci.* **2011**, *4*, 421−424.
(67) Koh, C. A.; Wisbey, R. P.; Wu, X.; Westacott, R. E.; Soper, A. K. Water ordering around methane during hydrate formation. *J. Chem. Phys.* **2000**, *113*, 6390−6397.
(68) Chialvo, A. A.; Houssa, M.; Cummings, P. T. Molecular Dynamics Study of the Structure and Thermophysical Properties of Model sI Clathrate Hydrates. *J. Phys. Chem. B* **2002**, *106*, 442−451.
(69) Geng, C. Y.; Hao, W.; Han, Z. Molecular simulation of the potential of methane reoccupation during the replacement of methane hydrate by CO_2. *J. Phys. Chem. A* **2009**, *113*, 5463−5469.
(70) Teich-McGoldrick, S. L.; Greathouse, J. A.; Jové-Colón, C. F.; Cygan, R. T. Swelling Properties of Montmorillonite and Beidellite Clay Minerals from Molecular Simulation: Comparison of Temperature, Interlayer Cation, and Charge Location Effects. *J. Phys. Chem. C* **2015**, *119*, 20880−20891.
(71) Li, X.; Li, Q.; Yang, S.; Yang, G. Swelling of Clay Minerals: Dual Characteristics of K^+ ions and Exploration for Critical Influence Factor. *Phys. Chem. Chem. Phys.* **2019**, *21*, 1963−1971.
(72) Zhang, L.; Lu, X.; Liu, X.; Zhou, J.; Zhou, H. Hydration and Mobility of Interlayer Ions of (Na_x, Ca_y)-Montmorillonite: A Molecular Dynamics Study. *J. Phys. Chem. C* **2014**, *118*, 29811−29821.
(73) Breslow, R. Hydrophobic Effects on Simple Organic Reactions in Water. *Acc. Chem. Res.* **1991**, *24*, 159−164.
(74) Jiménez-Ángeles, F.; Firoozabadi, A. Hydrophobic Hydration and the Effect of NaCl Salt in the Adsorption of Hydrocarbons and Surfactants on Clathrate Hydrates. *ACS Cent. Sci.* **2018**, *4*, 820−831.
(75) Yan, K.-F.; Li, X.-S.; Chen, Z.-Y.; Xia, Z.-M.; Xu, C.-G.; Zhang, Z. Molecular dynamics simulation of the crystal nucleation and growth behavior of methane hydrate in the presence of the surface and nanopores of porous sediment. *Langmuir* **2016**, *32*, 7975−7984.
(76) Jorgensen, W. L.; Madura, J. Temperature and size dependence for Monte Carlo simulations of TIP4P water. *Mol. Phys.* **1985**, *56*, 1381−1392.
(77) Chang, F.-R. C.; Skipper, N. T.; Sposito, G. Monte Carlo and Molecular Dynamics Simulations of Interfacial Structure in Lithium-Montmorillonite Hydrates. *Langmuir* **1997**, *13*, 2074−2082.
(78) Varma, S.; Rempe, S. B. Coordination numbers of alkali metal ions in aqueous solutions. *Biophys. Chem.* **2006**, *124*, 192−199.

https://dx.doi.org/10.1021/acsearthspacechem.9b00323
ACS Earth Space Chem. 2020, 4, 572−582